Tuning Superconductivity in Nanosecond Laser-Annealed Boron-Doped Si 1– x Ge x Epilayers

Shimul Kanti Nath, Ibrahim Turan, Léonard Desvignes, Ludovic Largeau, Olivia Mauguin, Marc Túnica, Michele Amato, Charles Renard, Géraldine Hallais, Dominique Débarre, et al.

Tuning superconductivity in nanosecond laser annealed boron doped $Si_{1-x}Ge_x$ epilayers

S. Nath,[1] I. Turan,[1] L. Desvignes,[1] L. Largeau,[1] O. Mauguin,[1] M. Túnica,[2]
M. Amato,[2] C. Renard,[1] G. Hallais,[1] D. Débarre,[1] and F. Chiodi[1,*]

[1] *Uni. Paris-Saclay, CNRS, Centre de Nanosciences et de Nanotechnologies, 91120, Palaiseau, France*
[2] *Uni. Paris-Saclay, CNRS, Laboratoire de Physique des Solides, 91405 Orsay, France*

(Dated: June 14, 2024)

Superconductivity in ultra-doped $Si_{1-x}Ge_x : B$ epilayers is demonstrated by nanosecond laser doping, which allows introducing substitutional B concentrations well above the solubility limit and up to 7 $at.\%$. A Ge fraction x ranging from 0 to 0.21 is incorporated in $Si : B$: 1) through a precursor gas by Gas Immersion Laser Doping; 2) by ion implantation, followed by nanosecond laser annealing; 3) by UHV-CVD growth of a thin Ge layer, followed by nanosecond laser annealing. The 30 nm and 75 nm thick $Si_{1-x}Ge_x : B$ epilayers display superconducting critical temperatures T_c tuned by B and Ge between 0 and 0.6 K. Within BCS weak-coupling theory, T_c evolves exponentially with both the density of states and the electron-phonon potential. While B doping affects both, through the increase of the carrier density and the tensile strain, Ge incorporation allows addressing independently the lattice deformation influence on superconductivity. To estimate the lattice parameter modulation with B and Ge, Vegard's law is validated for the ternary SiGeB bulk alloy by Density Functional Theory calculations. Its validity is furthermore confirmed experimentally by X-Ray Diffraction. We highlight a global linear dependence of T_c vs. lattice parameter, common for both $Si : B$ and $Si_{1-x}Ge_x : B$, with $\delta T_c/T_c \sim 50\,\%$ for $\delta a/a \sim 1\,\%$.

I. INTRODUCTION

SiGe is a key material for micro-electronics. The possibility to combine classical SiGe technology with quantum circuits is thus appealing to exploit the large-scale integration and reproducibility associated with CMOS devices [1]. Hole spin qubits have been developed in Ge/SiGe quantum dots [2] and SiGe nanowires [3, 4], taking advantage from the control on the environment and the low nuclear spin possible in group IV materials. Furthermore, Ge and SiGe have been incorporated in Josephson field effect transistors [4, 5], hosted transmon qubits, and their microwave losses have been investigated [6]. The possibility of inducing superconductivity directly in thin SiGe layers might furthermore provide an advantage in coupling SiGe-based classical electronics to superconducting quantum circuits.

It has been shown that Silicon displays a superconducting phase when ultra-doped with B [7–10]. An extreme boron doping concentration is required to trigger superconductivity in SiB, more than three times the solubility limit. This concentration, impossible to reach using conventional micro-electronic processes, was obtained using Gas Immersion Laser Doping (GILD), an out-of-equilibrium technique combining chemisorption of a precursor gas in a Ultra-High-Vacuum environment, and nanosecond laser annealing [10–12]. In this paper, we employ GILD to ultra-dope with B thin SiGe layers, demonstrating the realisation of a superconducting phase.

In addition to the intrinsic interest of SiGe superconductivity, the investigation of the evolution of the superconducting critical temperature T_c with both B and Ge doping allows to better understand what triggers superconductivity in Si and SiGe. Indeed, BCS theory in the weak coupling limit expects T_c to exponentially increase with the electron-phonon coupling $\lambda = N(E_F)V_{e-ph}$, the product of the electron-phonon potential V_{e-ph} and the density of states at Fermi energy $N(E_F)$. B doping modifies both $N(E_F)$ and V_{e-ph}: $N(E_F)$ is related to n_B, as evident in the frame of the 3D free electron model where $N(E_F) \propto (3\pi^2 n_B)^{1/3}$. In addition, due to the smaller size of B compared to Si, an important lattice deformation up to $\delta a/a = -3.5\,\%$ is induced at the same time [8], affecting the phonon frequencies involved in Cooper pairing. The incorporation of Ge makes it possible to modify, solely and independently, the lattice deformation, allowing to elucidate the relevant parameters that govern superconductivity.

II. ULTRA DOPED $Si_{1-x}Ge_x : B$

A. Gas Immersion Laser Doping

To attain the extremely high doping levels necessary to induce superconductivity, we employ fast liquid phase epitaxy, characterized by recrystallisation times of a few tens of nanoseconds (see Methods). A puff of the precursor gas (BCl_3 or $GeCl_4$) is injected onto the substrate surface, saturating the chemisorption sites, so that the supply of incorporated atoms is constant and self-limited. A pulse of excimer XeCl laser (λ = 308 nm, pulse duration 25 ns) melts the substrate, and the chemisorbed atoms diffuse in the liquid. At the end of the laser pulse, an epitaxial out-of-equilibrium recrystallisation takes place from the substrate at a speed of $\sim 4\,$m/s [13], achieving concentrations larger than the solubility limit ($\sim 1\,at.\%$ for B in Si). The laser energy density, tuned

* Corresponding author: francesca.chiodi@c2n.upsaclay.fr

Type of Ge incorporation	Thickness (nm)	Laser shots B	C_B (at.%)	Laser shots Ge	C_{Ge} (at.%)
GILD - 5	30	30-400	2.3 - 10.6	5	0.27
GILD - 15	30	30-400	2.3 - 10.6	15	0.8
GILD - 200	30	160-475	8 - 11.2	200	10.7
GILD - Ge	30	220	9.2	5-400	0.27-21.3
Ge CVD	30	30-400	2.3 - 10.6	-	17.1
Ge implanted ($10^{15}\,cm^{-2}$)	75	3 - 258 + B impl. ($5\times10^{15}\,cm^{-2}$)	1.5 - 10.8	-	0.27
Reference SiB	30	50-400	3.6 - 10.6	-	-

TABLE I. Details on the SiB and SiGeB sample series investigated in this work: Ge incorporation method, thickness, number of nanosecond laser annealing repetitions, total B and Ge concentrations C_B and C_{Ge} in atomic %.

with an attenuator, controls the melted thickness in the 5-500 nm range. A flat, straight, and sharp (few nm thick) interface is created between the ultra-doped layer and the substrate. In order to control the amount of B and Ge incorporated, the entire chemisorption-melting-crystallisation process is repeated the desired number of times (number of laser shots N). The total B (Ge) concentration C_B (C_{Ge}) is proportional to the number of GILD process repetitions N [14–16] (see Methods for previous works detailing the calibration of the thickness and of B and Ge concentrations).

B. Ge incorporation

We explore the low temperature electrical characteristics of thin $Si_{1-x}Ge_x$:B films, ultra-doped in boron (B) by Gas Immersion Laser Doping. Three different methods are used to incorporate the Ge and control its amount: 1) Gas Immersion Laser Doping with $GeCl_4$ as a precursor gas; 2) Implantation of Ge and B, followed by nanosecond laser annealing; 3) Growth by UHV-CVD of a thin Ge layer, followed by nanosecond laser annealing.
N-type Si substrates of resistivity $50\,\Omega cm$ are used for all sample series. The substrates are introduced in the UHV chamber after an acetone and ultrasounds cleaning to remove organic surface contamination, and 1 minute Buffered Hydrofluoric acid etch to remove the native silicon oxide.

1) Gas Immersion Laser Doping of Ge
Four samples series are realised by GILD (see Table I): three with varying B content and a fixed Ge concentration (GILD-5, GILD-15, GILD-200), and one with a varying Ge content and fixed B concentration (GILD-Ge). The doped thickness is $t = 30\,$nm, corresponding to a melting time of 30 ns on undoped Si by a laser energy density at the sample level of $1000\,\mathrm{mJ/cm^2}$. B atoms have a high diffusion coefficient in the liquid Si ($D \sim 10^{-4}\mathrm{cm^2/s}$) and a segregation coefficient near 1 at the high crystallisation speeds attained ($k = 0.95$) [17], insuring a homogeneous B distribution within the recrystallised layer even for the longer annealing processes ($\sim 15\,\mu$s for 500 cycles of 30 ns). Thus, a homogeneous distribution is expected even when the B is further submitted to the subsequent process time of the Ge incorporation. In contrast, a graded profile is expected for Ge, accumulating towards the surface and depleting the bottom of the layer, an effect of the smaller segregation coefficient ($k \sim 0.6 - 0.8$) [18].
2) Nanosecond Laser Annealing of implanted Ge and B
In one sample series (Ge implanted), an implantation step prior to the nanosecond laser annealing is employed to introduce a Ge dose of $10^{15}\,cm^{-2}$, and right afterwards a small B dose ($5\times10^{15}\,cm^{-2}$, equivalent to 42 laser shots, i.e. 1.25 at.%). The following GILD processes serve both the purposes of incorporating in substitutional sites the implanted B and Ge and increasing the B doping. This series is thicker than the rest of this work ($t = 75\,$nm) to ensure that the implanted atoms, including the implantation queue, are within the melted depth.
3) Nanosecond Laser Annealing of a thin CVD Ge layer
In one sample series (Ge CVD), the Ge is supplied from an epitaxially grown thin Ge layer. The following GILD processes serve the purpose of melting the Ge and the Si underneath, mixing them, and of introducing the B doping. The epitaxial growth of Ge on Si is carried out in an UHV-CVD system with a base pressure of 10^{-10} mbar. Pure SiH_4 and GeH_4 diluted at 10% in H_2 are used as gas sources. The growth time is settled at 20 min in order to achieve 6 nm of Ge [19, 20] (see Methods for further details).

III. SUPERCONDUCTIVITY IN $Si_{1-x}Ge_x : B$

A. Low temperature measurements

At the end of the B and Ge incorporation, Ti(15 nm)/Au(150 nm) metallic contacts for 4-points measurements are deposited over the doped layers by laser lithography and e-beam evaporation. The resistance R of a region $150\,\mu$m wide and $300\,\mu$m long is extracted from dc V(I) measurements of averaged positive and negative bias current (I_{dc}=10 to 50 nA). R is recorded as a function of temperature (300 K to 0.05 K) and perpendicular magnetic field (0 to 55 mT) in an Adiabatic Demagnetisation Refrigerator setup. After the demagnetisation and relative cool down, the system is left to evolve dur-

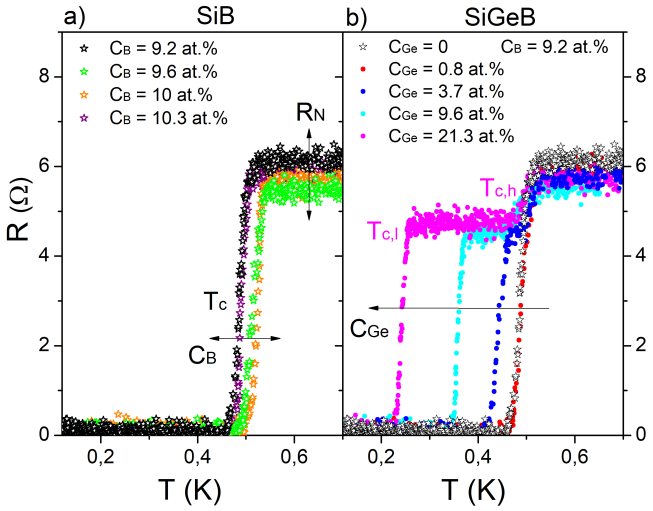

FIG. 1. Typical resistance R vs. temperature T superconducting transitions for a) the Reference SiB GILD samples series, containing no Ge and a variable B concentration $C_B = 9.2 - 10.3$ at.%; b) SiGeB layers from the GILD-Ge sample series, with constant $C_B = 9.2$ at.% and varying Ge concentration $C_{Ge} = 0.8 - 21.3$ at.%. $T_{c,h}$ and $T_{c,l}$ indicate respectively the high and low temperature transition for SiGeB at high doping.

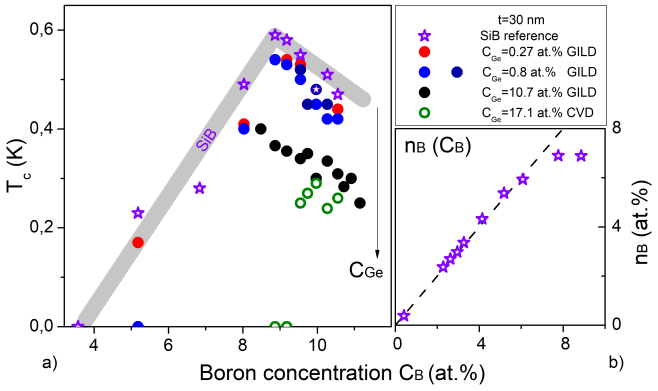

FIG. 2. a) SiB and SiGeB superconducting critical temperature T_c at mid-transition vs. total B concentration C_B for sample series GILD-5, GILD-15, GILD-200, Ge CVD and Reference SiB. All series are 30 nm thick. SiGeB samples present two transitions at the highest C_{Ge}. In this case, the one leading to the zero resistance state, $T_{c,l}$, is plotted. b) Hole carrier density n_B (substitutional B concentration) vs. total B concentration C_B extracted from Hall measured in a dedicated SiB sample series with t=30 nm. C_B is measured from SIMS (Secondary Ion Mass Spectrometry) concentration profiles over the layer thickness t: $C_B = \frac{\int C_{SIMS}\, dt}{t}$. The grey line is a guide to the eye for SiB (no Ge) evolution.

ing the slow (∼1.5 hours) temperature increase, giving a precise evaluation of the superconducting transition temperature. For the transitions in presence of a magnetic field B, the demagnetisation is stopped at B (instead of decreasing to zero field as in usual demagnetisation cycles), so that the transition is recorded in presence of a constant magnetic field.
In order to access the hole carrier density, Hall bars are realised in a separate reference SiB sample series (see Methods).

B. Superconductivity evolution with B in $Si:B$

Fig. 1-a shows typical $R(T)$ superconducting transitions for the Reference SiB samples series, containing no Ge, with varying total B concentration C_B. The $R(T)$ curves show a single, relatively sharp transition, of width $\Delta T \sim 0.08$ K∼ 16%. We observe that the superconducting critical temperature T_c and the normal state resistance R_N evolve with C_B, the total amount of B incorporated. Varying C_B results in a modification of the hole carrier density n_B. For $C_B < 6\, at.\%$, all B atoms are substitutional, providing a hole carrier, and we obtain 100% activation, with $n_B = C_B$ (Fig. 2-b). For $C_B > 6\, at.\%$, the activation progressively lowers with the gradual increase of inactive B complexes, and n_B increase slows down. Finally, at $C_B > 9.5$ at.%, n_B saturates, as a result of the formation of B aggregates [16, 21]. As a consequence, R_N initially decreases with C_B in the full activation regime, while at higher doping it saturates and slowly increases following the increase of disorder and formation of aggregates [16]. In the parameter range of this work, we are close to R_N saturation, and only little variations are observed when modifying C_B (see Fig. 1a).
The evolution of T_c with C_B is instead marked. T_c initially increases roughly linearly with C_B, to attain a maximum at $C_B = 8.9\, at.\%$, and then decreases, more slowly, in the saturation regime (Fig.2-a). The similar evolution of $T_c(C_B)$ and $n_B(C_B)$ suggests that T_c is controlled by the active concentration n_B. However, we observe that T_c keeps increasing with C_B even *after* the saturation of the hole concentration n_B at $C_B = 7.8\, at.\%$. Thus, the question arises if superconductivity in silicon, besides being controlled by the carrier density, might be tuned through the strain induced, at the same time, by the smaller B atoms. The demonstration of superconductivity in SiGe by ultra-doping with B, in addition to its intrinsic interest associated to the role played by SiGe in classical (and quantum) electronics, opens the way to an experimental answer to this question. The independent incorporation of B and Ge allows indeed to address, independently, the role of the carrier concentration and the strain in the evolution of superconductivity.

C. Superconductivity evolution with Ge and B in $Si_{1-x}Ge_x:B$

Fig. 1-b shows the $R(T)$ superconducting transitions of typical SiGeB layers from the GILD-Ge sample

series, with constant $C_B = 9.2\,\text{at.\%}$ and varying Ge concentration $C_{Ge} = 0.8 - 21.3\,\text{at.\%}$. While at small Ge content the transitions are nearly on top of the Reference SiB, single, transition, for higher C_{Ge} the curves show two transitions. The first transition, $T_{c,h}$, at higher temperature, accounts for $23 - 24\,\%$ of the resistance drop. The second transition, accounting for $\sim 75\%$ of the resistance, is similarly sharp, with $\Delta T \sim 0.05\,\text{K} \sim 13\%$, and is characterized by a lower transition temperature $T_{c,l}$. The decrease of $T_{c,l}$ with Ge concentration observed in Fig. 1-b is a general occurrence for all B concentrations, and not particular to the fixed C_B of the curves displayed. Indeed, as shown in Fig. 2, $T_{c,l}(C_B)$ follows for each SiGeB series (GILD-5, GILD-15, GILD-200, Ge CVD) a dependence that mimics that of SiB, but shifted towards lower T_c values, with a shift that increases with C_{Ge}. A strong disorder induced by the Ge incorporation might explain such $T_{c,l}$ reduction. However, an important disorder would be evident in the normal state square resistance at low temperature, $R_{N,sq} \sim 3\,\Omega$, which instead remains well below the resistance quantum (see Fig. 1). Moreover, R_N is only little affected by the Ge incorporation, and a slight R_N reduction with C_{Ge} is even observed, probably related to a better carrier mobility in SiGe despite the scattering induced by Ge random position in the lattice. Thus, the large T_c suppression ($\delta T_{c,l}/T_{c,l} \sim 50\,\%$) cannot be explained by the low disorder ($\delta R_N/R_N \sim 10\,\%$).

Fig. 3 shows the evolution of $T_{c,l}$ and $T_{c,h}$ as a function of the Ge concentration for the sample series GILD-Ge. $T_{c,h}$ is on average constant, globally independent of the nominal Ge content, and its value is consistent within 7% with the T_c expected, in the absence of Ge, for a SiB layer of the same B doping. In addition, the measured critical magnetic field $H_{c2,h}$, is also compatible with the SiB reference, $H_{c2} \sim 200$ to $1000\,\text{G}$ in the C_B range examined. Fitting $H_{c2,h}(T)$ (see Methods), it is possible to extract the superconducting coherence length $\xi_{SiGeB,h}$. For $C_B = 9.2\,at.\%$ and $C_{Ge} = 8 - 21.3\,at.\%$, we find $\xi_{SiGeB,h} = 59 - 65\,\text{nm}$, similar to SiB $\xi_{SiB} = 60\,\text{nm}$ but with $\sim 10\,\%$ larger value associated to a higher diffusion coefficient (as also observed in R_N). In contrast we find, for the low temperature transition $T_{c,l}$ of the same samples, a strong dependence with C_{Ge}, a suppressed $H_{c2,l} \sim 150$ to 350 G, and a larger $\xi_{SiGeB,l} = 95 - 140\,\text{nm}$ varying with C_{Ge}, the result of a roughly doubled diffusion coefficient as compared to ξ_{SiB}.

Thus, while at low Ge content we observe the behaviour of a homogeneous SiGeB layer, two regions are present at high Ge content: one depleted in Ge, behaving as pure SiB with only slight variations as a result of the Ge incorporation processes, the other deeply affected by the incorporated Ge, with a doubled diffusion coefficient and a suppressed T_c. The ratio of the two regions volumes can be estimated from the height of the two resistance steps and the diffusion coefficients extracted from the measured coherence lengths. This results in a Ge-poor region about 6 times smaller than the nominal Ge region.

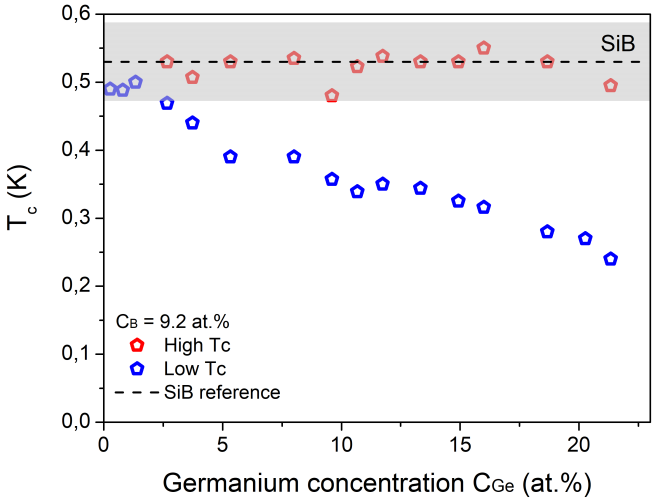

FIG. 3. Superconducting critical temperatures of the two resistive transitions $T_{c,l}$ (blue) and $T_{c,h}$ (red) observed in SiGeB series GILD-Ge (see Fig.1), for a fixed $C_B = 9.2\,at.\%$ and as a function of Ge concentration C_{Ge}. The dotted line corresponds to the T_c of the Reference SiB sample with $C_B = 9.2\,at.\%$ and no Ge, realised in the same run as the GILD-Ge series. The grey line is a guide to the eye.

D. Superconductivity evolution with lattice deformation

In order to understand the role of Ge on SiGeB superconductivity, and as Ge concentration does not directly affect the carrier concentration, we focus on the structural properties of the layer. In particular, we examine the deformation induced by both the Ge-induced compressive strain and the opposite B-induced tensile strain in selected samples from the GILD-Ge series and the respective Reference SiB sample. X-Ray Diffraction maps around the (224) reflection are realised to image both the in-plane and out-of-plane layer deformations (see Methods). Two samples are shown in Fig. 4: a SiB layer, with $C_B = 9.2\,at.\%$, and a SiGeB layer, with the same C_B and $C_{Ge} = 10.7\,at.\%$. The SiB layer is partially relaxed, with an in-plane lattice constant smaller than that of the Si substrate, as visible from the larger Q_x wavevector in SiB as compared to Si. However, upon incorporation of Ge, the layer evolves back to a nearly fully strained configuration, with only the beginning of strain relaxation. This is the result of Ge partially compensating the B induced strain, as $a_{Ge} = 5.6578\,\mathring{A} > a_{Si} = 5.4307\ \mathring{A} > a_B = 3.74\ \mathring{A}$ [22]. From the in-plane and out-of-plane wavevectors Q_x and Q_z, we extract the lattice parameter of the SiB (SiGeB) layers, reported in Fig. 4-a, with $(Q_{Si} - Q_{SiB})/Q_{SiB} = (a_{SiB} - a_{Si})/a_{Si}$

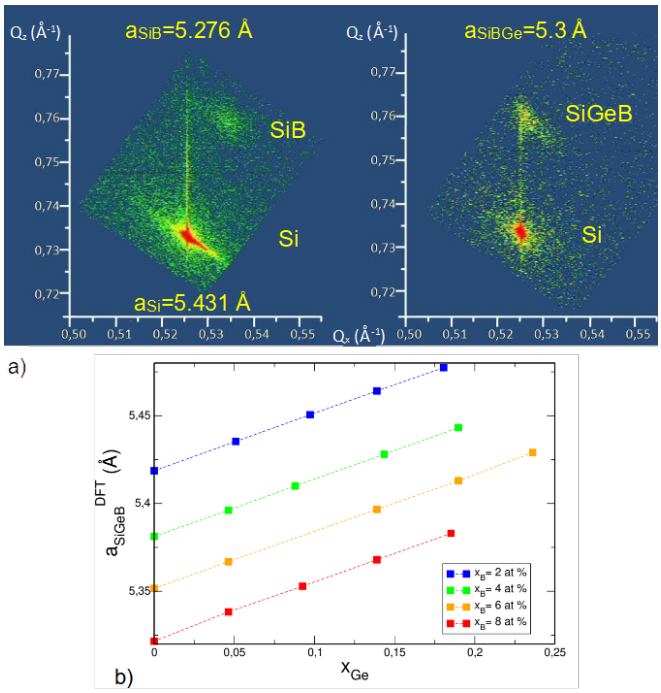

FIG. 4. a) XRD reciprocal maps along (224) direction for (left) a SiB sample with $C_B = 9.2\,at.\%$ from Reference SiB series and (right) a SiGeB sample with $C_B = 9.2\,at.\%$ and $C_{Ge} = 10.7\,at.\%$ from GILD-Ge series. Intensity is depicted in colour contrast, with cold colours for the lower signal and hot colours for higher intensities. Q_x and Q_z correspond to the in-plane and out-of-plane wavevectors. The lattice parameter extracted from the XRD measurements is noted on each image. b) Optimized lattice constant for the ternary SiGeB bulk alloy calculated within Density Functional Theory (DFT) in the generalized gradient approximation (GGA) as a function of the Ge fraction, x_{Ge} and for different values of the B fraction, x_B. The x_{Ge} value lies in the range of 0 to 25 $at.\%$ while x_B varies between 2 and 8 $at.\%$.

and $Q = \sqrt{Q_x^2 + Q_z^2}$.

Having established the experimental lattice parameters available from the limited number of XRD maps, we explore their dependence on B and Ge concentration by performing Density Functional Theory (DFT) calculations in the generalized gradient approximation (GGA) for the ternary SiGeB bulk alloy. Special Quasi Random Structure approach [23] is used to extract from the ensemble of all the possible random configurations only those which provide the most accurate approximation to the true random alloys. Further details of the DFT simulations are presented in the Methods section. For the pure SiGe alloy we find that, in the low Ge concentration regime, the behaviour of the lattice constant follows the Vegard's law for binary semiconductors [24, 25]. Indeed, the DFT calculated lattice parameter of the alloy linearly increases with Ge fraction x_{Ge}, according to $a_{SiGe} = a_{Si} \cdot x_{Si} + a_{Ge} \cdot (1 - x_{Si})$, where a_{Si}= 5.449 Å and a_{Ge}= 5.789 Å are the DFT-GGA lattice parameter of pure Si and pure Ge, respectively. Once the pure SiGe alloy case analysed, we calculate the dependence of the lattice constant on the B concentration for the ternary SiGeB bulk alloy. We consider a B fraction, x_B, ranging from 2 $at.\%$ to 8 $at.\%$ and we vary the Ge composition from 0 to 25 $at.\%$, matching the experimental parameter range. As is shown in Fig. 4-b, increasing x_B lowers the value of a_{SiGe} while maintaining the linear Vegard's behaviour. These results demonstrate that, in this chemical composition regime, the use of a linear interpolation of the three alloy components is theoretically justified and can be summarized in the following equation:

$$a_{SiGeB} = a_B \cdot x_B + a_{Ge} \cdot x_{Ge} + a_{Si} \cdot (1 - x_B - x_{Ge}) \quad (1)$$

where a_B is determined through a constrained fit (with a_{Si} and a_{Ge} fixed to their GGA values) to be 3.81 Å, which is in very good agreement with the experimental value measured in Ref. [22]. Even though, due to the well-known GGA underbinding tendency [26], the simulated pure elements lattice parameters are slightly overestimated if compared with the experimental values (by a few percent difference), the theoretical results fully validate Eq.1.

We thus employ Vegard's law (Eq. 1) as a function of x_B and x_{Ge} to predict the lattice parameters of the samples shown in Fig. 4, by taking as input the experimental values of C_B and C_{Ge} and the experimentally determined $a_{Si} = 5.4307$ Å, $a_{Ge} = 5.6578$ Å and $a_B = 3.74$ Å, the B and Ge fractions $x_j = C_j / n_{Si}$ being calculated in respect to the pure Si density $n_{Si} = 5 \times 10^{22}\,cm^{-3}$. For the samples analysed in Fig. 4, we obtain $a_{SiB} = 5.2755$ Å(vs. $a_{SiB,XRD} = 5.276 \pm 0.005$ Å), and $a_{SiGeB} = 5.300$ Å(vs. $a_{SiGeB,XRD} = 5.299 \pm 0.005$ Å), an excellent agreement, well within the error associated to 'pointing' uncertainty on the XRD maps.

With both experimental and numerical validation, we extend the 3-elements Vegard's law to calculate the lattice parameters a for the samples for which no XRD is available. To correctly estimate a_{SiB} and a_{SiGeB}, only the substitutional dopant concentration providing a lattice deformation is relevant. We thus exclude from the following analysis the samples with $C_B > 9.2\,at.\%$, the concentration range where aggregates appear, rendering inaccurate the estimation of the substitutional concentration [21]. The concentration range between the fully activate regime and the saturation regime $6\,at.\% < C_B \leq 9.2\,at.\%$ is however included, as the still-high activation (ratio of active to total B concentration $> 75\,\%$) is limited in this region by substitutional inactive B complexes formed by a few atoms (B dimers, trimers) [16]. Such complexes also induce a lattice deformation, whose value differs however from that of isolated B atoms [27, 28]. We thus might expect a maximum error of $\sim 20\,\%$ on the deformation estimation for these complexes, but, as they account at most for 25 % of C_B (and only at the highest concentrations), the final induced error on the lattice parameter is expected within a few %. In the case of Ge, the whole C_{Ge} range is considered, as for the concentrations investigated here, Ge is expected to be fully substitutional [18].

The dependence of T_c on the lattice parameter a calculated from C_B and C_{Ge} is shown in Fig. 5 for Reference SiB series, GILD-5, GILD-15, GILD-200, GILD-Ge and Ge implanted. It is remarkable that all sample series collapse in a common linear trend: SiB samples see their lattice parameter decrease with B doping and 'move' towards higher T_c from right to left; SiGeB samples with a fixed C_B see the lattice parameter increase due to the Ge incorporation, and move from left to right to lower T_c, over SiB samples with smaller B concentrations. The multiple methods employed to incorporate the Ge do not seem to affect significantly the global result, and neither does the difference between the 30 nm and 75 nm thick samples series. The series to series deviations from the average $T_c(a)$ observed in Fig. 5 are associated to uncertainties in the lattice parameter of $\delta a/a \sim 0.7\,\%$, and can be traced back to the uncertainty in the determination of the deformation associated to the few-atoms complexes. It is noteworthy that modifying the lattice parameter by $\delta a/a = -1\,\%$ leads to a large change in the superconducting critical temperature of $\delta T_c/T_c = 50\,\%$. A strong dependence of T_c with the lattice parameter is reported for other superconductors, such as In_xTe [29] or covalent superconductors (like Si and SiGe), such as superconducting B doped diamond ($\delta T_c/T_c \sim 64\,\%$ for $\delta a/a \sim 0.2\,\%$) [30] or K_3C_{60} and Rb_3C_{60} fullerenes ($\delta T_c/T_c \sim 83\,\%$ for $\delta a/a \sim 4\,\%$) [31].

Such strong increase of T_c upon the reduction of the lattice parameter might be associated to the increase of the electron-phonon potential V_{e-ph}, increasing in turn the electron-phonon coupling λ, and thus the T_c. Superconductivity in ultra-doped SiB and GeB was indeed predicted in isotropic crystalline structures by ab-initio calculations as the result of phonon modes softening [32]. A good agreement was found with relaxed SiB layers realised by GILD, even though the superconductivity threshold could not be correctly modelled and was shown to depend on the lattice deformation [16]. The incorporation of Ge in the SiB lattice by nanosecond laser annealing allows addressing specifically the electron-phonon potential independently of the density of states, through the finely tuned lattice parameter, and will help clarifying the role of lattice deformation in covalent Si and SiGe superconductors.

IV. CONCLUSIONS

In conclusion, we demonstrate superconductivity in $Si_{1-x}Ge_x : B$ epilayers by nanosecond laser ultra-doping with B. The B concentration reached, well above the solubility limit thanks to such out-of-equilibrium technique, is varied from $C_B = 1.5$ to $11\,at.\%$, with 100% activation rate below $C_B = 6\,at.\%$ and over 75% up to $C_B = 9.2\,at.\%$. The Ge fraction explored is x =0 to 0.21. Ge is incorporated in three different ways: 1) through a precursor gas by Gas Immersion Laser Doping; 2) by ion implantation, followed by nanosecond laser annealing; 3) by UHV-CVD growth of a thin Ge layer, followed by nanosecond laser annealing. The 30 nm and 75 nm thick SiGeB epilayers display a zero resistance state, with superconducting critical temperature T_c varying with B and Ge concentration from 0 to 0.6 K, a superconducting critical field H_{c2} = 150 to 500 G, and a superconducting coherence length ξ = 70 to 140 nm, larger than SiB layers of equal concentration due to a doubled diffusion coefficient associated to Ge incorporation. To understand the T_c evolution, we turn towards BCS theory, which predicts a T_c exponential evolution with the electron-phonon coupling constant $\lambda = N(E_F)V_{e-ph}$, the product of the density of state at Fermi level and the electron-phonon interaction potential. Starting with the simplest SiB alloy, we observe an initial increase of T_c with C_B, that can be associated to the increase of the charge carrier density ($n_B = 1.5-7\,at.\%$), and as a consequence of $N(E_F)$. However, T_c keeps increasing even when the hole concentration n_B saturates at $C_B = 7.8\,at.\%$, as a result of the formation of B aggregates. We thus explore the role played by the structural deformations on superconductivity, by fine-tuning the strain through the modulation of the Ge concentration at fixed carrier density. To estimate the lattice parameter modulation with B and Ge, we validate Vegard's law for the ternary SiGeB bulk alloy by DFT-GGA calculations. The theory is in excellent agreement with X-Ray Diffraction maps, where both the in-plane and the out-of-plane lattice deformation is measured. By correlating the T_c with the calculated lattice parameter, we observe a global linear dependence, common for both SiB and SiGeB layers, and independent on the Ge incorporation method or on the sample thickness, with $\delta T_c/T_c \sim 50\,\%$ for $\delta a/a \sim 1\,\%$, highlighting the importance of structural strain, at fixed carrier concen-

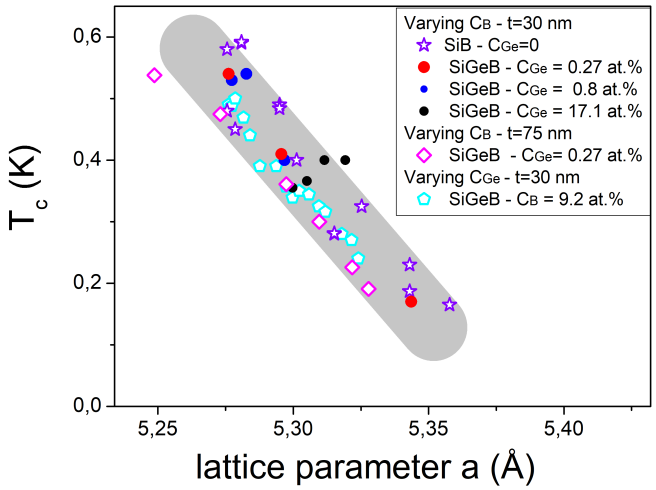

FIG. 5. Superconducting critical temperature vs. lattice parameter calculated with Eq.1 for Reference SiB series, GILD-5, GILD-15, GILD-200, GILD-Ge and Ge implanted (see Table I All series are plotted, for $C_B \leq 9.2\,at.\%$, to avoid the region where B aggregates are present, affecting the estimation of the lattice parameter.

tration.

Acknowledgements

We are grateful for support from the French CNRS RENATECH network, the Physical Measurements Platform of University Paris-Saclay, the French National Research Agency (ANR) under Contract No. ANR-16-CE24-0016-01, ANR-19-CE47-0010-03 and ANR-22-QUA2-0002-02. M.A. and M. T. acknowledge the ANR AMPHORE project (ANR-21-CE09-0007).

Methods

1. Gas Immersion Laser Doping

GILD is performed in an ultra high vacuum (UHV) reactor of base pressure $10^{-9}-10^{-10}$ mbar, to ensure a minimal impurity incorporation during the melt phase. The working pressure of the precursor gas is $p \sim 10^{-5} mbar$, high enough to saturate the chemisorption sites and low enough that photolytic or pyrolytic CVD processes are avoided.
After the laser melting, the crystallisation front proceeds towards the surface where the excess impurities contained in the liquid are expelled, such as Cl whose segregation coefficient is close to 0 [33].
Thanks to a careful optical treatment of the laser beam, the energy density at the 2x2 mm^2 sample level has $\sim$1.2% spatial homogeneity. This ensures the homogeneity of the layer thickness, resulting in a flat and straight interface of the SiGe with the substrate.
Since the laser absorption is sensitive to the layer doping level, a fixed laser energy results in an increasing layer depth. In order to obtain a constant doped depth independent of the B or Ge content, we measure the layer time-resolved reflectometry, and maintain a constant melt time during the doping by decreasing progressively the laser energy [34]. For instance, the initial energy value for a melt duration of 30 ns (melt depth of 30 nm) is 1000 mJ/cm^2. During B doping, the energy is decreased by 13% for 80 laser shots ($n_B = 5.2at.\%$) and by 19% for 220 laser shots. During Ge doping, the required energy variation is smaller, within a few %. The values of the energy decrease for each doping are common for all the GILD series, Reference SiB and the Ge implanted series. When both B and Ge are introduced by GILD, B doping is performed before the Ge incorporation. Indeed, a homogeneous B distribution is expected even when the B is further submitted to the subsequent process time of the Ge incorporation. In contrast, the Ge profile is expected to evolve toward the surface during the anneal, depleting the bottom of the layer [18]. To minimize the time spent by Ge atoms in the liquid phase, we thus incorporate GILD Ge last.
The thickness was calibrated extensively in past works [15, 21] against the laser energy density by Transmission Electron Microscopy, X-Ray Diffraction, and direct Scanning Electron Microscope visualisation of a cleaved SiB section, after selective etch of the undoped Si underneath. A careful calibration of the total B concentration was realised by Secondary Ion Mass Spectrometry (SIMS) in previous works for GILD samples [8, 15, 35] and for B-implanted samples followed by nanosecond laser anneal [9]. The active B concentration was calibrated by Hall measurements and X-Ray Diffraction (XRD) [15, 21]. The calibration of the Ge concentration was realised for GILD samples by Rutherford Backscattering Spectroscopy (RBS) both in random and channeling geometry, and confirmed by XRD for samples in the 40-235 nm thickness range and up to 18.5 at.% [18]. In samples where Ge is first deposited, then nanosecond laser annealed, the concentration was evaluated with RBS, EDX, TEM and XRD measurements [36, 37].

2. UHV-CVD growth of Ge/Si

The epitaxial growth of Ge on Si is carried out in an UHV-CVD system with a base pressure of 10^{-10} mbar. Pure SiH_4 and GeH_4 diluted at 10% in H_2 are used as gas sources. After a modified Shiraki chemical cleaning [38] the substrates are slowly annealed up to 700°C, the pressure being maintained below $7 \cdot 10^{-9}$ mbar. Afterwards, the chemical surface oxide is removed by flashing at 990°C, maintaining the low pressure. After the deposition of a Si buffer layer at 700°C under a pressure of $4 \cdot 10^{-4}$ mbar, the Ge heteroepitaxy at 330°C is initiated at a total pressure of $7 \cdot 10^{-3}$ mbar. The growth time is settled at 20 min in order to achieve 6 nm of Ge [19, 20].
During the GILD step to incorporate B, the laser energy is kept initially low and gradually increased over the last 10 process repetitions, in order to limit the time of Ge diffusion towards the surface and achieve a Ge profile as homogeneous as possible.

3. Hall measurements

The transverse voltage V_H is measured in a magnetic field perpendicular to the layer, at room temperature, with $V_H/I = \gamma \frac{B}{en_B t}$, $\gamma = 0.68$ the Hall mobility factor [39], I the bias current (10μA), B the applied magnetic field (0 to 2 T), e the electron charge and t the layer thickness.

4. Measurement of the critical magnetic field $H_{c2}(T)$

$R(T)$ superconducting transitions are measured for fixed values of a perpendicular magnetic field

from 0 to 55 mT. Both the SiB reference samples series and a few selected SiGeB samples are studied $[(C_B, C_{Ge}) = (9.2, 8)\,at.\%;\ (9.2, 21.3)\,at.\%;\ (8, 10.7)\,at.\%;\ (10.6, 10.7)\,at.\%]$. In the temperature range $T = 0.2 - 0.5\,\mathrm{K}$, SiB follows the expected trend for a thin superconducting film near T_c: $\mu_0 H_{c2} = \frac{3\Phi_0}{(2\pi^2\,\xi^2)}(1-\frac{T}{T_c})$. The extracted coherence length is $\xi = 60\,\mathrm{nm}$, in agreement with previous measurements [15]. The high temperature transition of SiGeB samples $T_{c,h}$, measured in the same temperature range, follows the same law, with $\xi = 59 - 65\,\mathrm{nm}$. These values, in agreement with SiB results, confirm the suppression of the Ge concentration in the region associated to $T_{c,h}$ (in stark contrast with $T_{c,l}$ behaviour). The slightly larger values might be a result of the supplementary processes to incorporate Ge. Indeed, the diffusion coefficient D affects ξ, as $\xi = \sqrt{(\hbar D/1.76 k_B T_c)}$.
The magnetic field dependence of the low temperature transition $T_{c,l}$ of SiGeB samples is also measured, showing a strong suppression of $H_{c2,l}$ with C_{Ge} and a larger $\xi = 70$ to $150\,\mathrm{nm}$, a result of an increased diffusion coefficient and a lower critical temperature.

5. X-Ray Diffraction

The diffractograms are realised with a Rigaku Smartlab XRD system with Cu-Kα1 radiation of wavelength $1.54056\,\mathring{A}$, operated at 45 kV and 200 mA. The x-ray beam is narrowed to measure only the central, homogeneous part of the laser annealed spot. To avoid the contribution of the gold contacts in the diffractogram, the contacts were removed by a KI Au-etch followed by 1 min dip in a 10% HF solution to remove Ti.

6. DFT simulations

DFT calculations were performed by using the SIESTA package [40] whose numerical atomic orbitals basis set allows treating large systems with an affordable computational cost. The exchange–correlation energy functional was approximated using the generalized gradient approximation (GGA) as implemented by Perdew, Burke, and Ernzerhof (PBE functional) [41]. Only valence electrons have been taken into account with core electrons being replaced by norm-conserving pseudopotentials of Troullier-Martins type. An optimized double-ζ polarized basis set was used for Si while a double-zeta plus two polarization orbitals (DZP2) basis set was chosen for both Ge and B. All the equilibrium ground state unit cells and geometries were obtained from conjugate-gradients structural relaxation using DFT forces through the Hellman-Feynman theorem. The structures were relaxed until the force on each atom was smaller than 0.01 eV/ Å. The cutoff of the grid used for the real space integration was set to 300 Ry while the self-consistent cycle tolerance for solving the Kohn-Sham equations was set to 10^{-4} eV. A uniform Monkhorst-Pack grid with 3×3×3 k-points was employed to sample the Brillouin zone. A supercell of 216 atoms was considered, which corresponds to a 3×3×3 supercell of the conventional 8-atom cell of bulk Si. To take into account the random nature of the alloy the Special Quasi Random Structure (SQS) approach [23] was adopted. The SQS configurations were generated using the ATAT code [42] and considering that each atom in the supercell can be replaced with a probability depending on its concentration, as shown in Ref. [43]. As a starting point, a pure Si supercell was considered and the Ge fraction of atoms was varied from 0 to 0.25 for several SQS configurations. For each of these configurations, the lattice parameter of the alloy was averaged over the different configurations and over the three cubic crystal axis to minimize the error due to numerical fluctuations during optimization. Once the pure SiGe alloys case was treated, the dependence of the lattice parameter on the B concentration was calculated. B concentrations from 2% to 8% and Ge composition from 0 to 25% were considered. All the studied systems are substitutional solid alloys in which Si, Ge, and B can occupy only substitutional lattice sites (interstitial are not taken into account).

[1] Andrea Ruffino, Tsung-Yeh Yang, John Michniewicz, Yatao Peng, Edoardo Charbon, and Miguel Fernando Gonzalez-Zalba. A cryo-cmos chip that integrates silicon quantum dots and multiplexed dispersive readout electronics. *Nat Electron*, 5:53–59, 2022.

[2] Nico W. Hendrickx William I. L. Lawrie Maximilian Russ Floor van Riggelen Sander L. de Snoo Raymond N. Schouten Amir Sammak Giordano Scappucci and Menno Veldhorst. A four-qubit germanium quantum processor. *Nature*, 591:580–585, 2021.

[3] Yongjie Hu, Ferdinand Kuemmeth, Charles M Lieber, and Charles M Marcus. Hole spin relaxation in ge–si core–shell nanowire qubits. *Nature nanotechnology*, 7(1):47–50, 2012.

[4] Michele Amato, Maurizia Palummo, Riccardo Rurali, and Stefano Ossicini. Silicon–germanium nanowires: chemistry and physics in play, from basic principles to advanced applications. *Chemical reviews*, 114(2):1371–1412, 2014.

[5] Florian Vigneau, Raisei Mizokuchi, Dante Colao Zanuz, Xuhai Huang, Susheng Tan, Romain Maurand, Sergey Frolov, Amir Sammak, Giordano Scappucci, Francois Lefloch, and Silvano De Franceschi. Germanium quantum-well josephson field-effect transistors and interferometers. *Nano Letters*, 19(2):1023–1027, 2019.

[6] Martin Sandberg, Vivekananda P. Adiga, Markus Brink, Cihan Kurter, Conal Murray, Marinus Hopstaken, John Bruley, Jason S. Orcutt, and Hanhee Paik. Investigating microwave loss of SiGe using superconducting transmon qubits. *Applied Physics Letters*, 118(12):124001, 03 2021.

[7] E. Bustarret, C. Marcenat, P. Achatz, J. Kacmarcik, F. Levy, A. Huxley, L. Ortega, E. Bourgeois, X. Blase, D. Débarre, and J. Boulmer. Superconductivity in doped cubic silicon. *Nature*, 444(7118):465–468, November 2006.

[8] C. Marcenat, J. Kacmarcik, R. Piquerel, P. Achatz, G. Prudon, C. Dubois, B. Gautier, J. C. Dupuy, E. Bustarret, L. Ortega, T. Klein, J. Boulmer, T. Kociniewski, and D. Débarre. Low-temperature transition to a superconducting phase in boron-doped silicon films grown on (001)-oriented silicon wafers. *Phys. Rev. B*, 81:020501, Jan 2010.

[9] A. Grockowiak, T. Klein, H. Cercellier, F. Lévy-Bertrand, X. Blase, J. Kačmarčik, T. Kociniewski, F. Chiodi, D. Débarre, G. Prudon, C. Dubois, and C. Marcenat. Thickness dependence of the superconducting critical temperature in heavily doped si:b epilayers. *Phys. Rev. B*, 88:064508, Aug 2013.

[10] Francesca Chiodi, Richard Daubriac, and Sébastien Kerdilès. Chapter 9 - laser ultra-doped silicon: Superconductivity and applications. In Fuccio Cristiano and Antonino La Magna, editors, *Laser Annealing Processes in Semiconductor Technology*, Woodhead Publishing Series in Electronic and Optical Materials, pages 357–400. Woodhead Publishing, 2021.

[11] PG Carey and TW Sigmon. In-situ doping of silicon using the gas immersion laser doping (gild) process. *Applied Surface Science*, 43(1-4):325–332, 1989.

[12] G Kerrien, J Boulmer, D Débarre, D Bouchier, A Grouillet, and D Lenoble. Ultra-shallow, super-doped and box-like junctions realized by laser-induced doping. *Applied Surface Science*, 186:45–51, January 2002.

[13] R.F. Wood and G.E. Jellison. Chapter 4 melting model of pulsed laser processing. volume 23 of *Semiconductors and Semimetals*, pages 165–250. Elsevier, 1984.

[14] A. Bhaduri, T. Kociniewski, F. Fossard, J. Boulmer, and D. Débarre. Optical and electrical properties of laser doped si:b in the alloy range. *Applied Surface Science*, 258(23):9228 – 9232, 2012. {EMRS} 2011 Spring Symp J: Laser Materials Processing for Micro and Nano Applications.

[15] Pierre Bonnet. *Mesures résonantes des propriétés hautes fréquences du silicium supraconducteur ultra-dopé au bore par laser*. Theses, Université Paris Saclay (COmUE), December 2019.

[16] Léonard Desvignes. *Laser ultra-doped superconducting silicon: from the material to the devices*. Theses, Université Paris Saclay , April 2023.

[17] R.F. Wood and F.W. Young. Chapter 5 nonequilibrium solidification following pulsed laser melting. volume 23 of *Semiconductors and Semimetals*, pages 251–312. Elsevier, 1984.

[18] Frédéric Fossard, Jacques Boulmer, Dominique Débarre, Jean-Luc Perrossier, Cyril Bachelet, Franck Fortuna, Véronique Mathet, and Daniel Bouchier. Pseudomorphic SiGe/Si(001) layers synthesized by gas immersion laser doping. *Applied Physics Letters*, 93(2):021911, 07 2008.

[19] M. Halbwax, D. Bouchier, V. Yam, D. Débarre, Lam H. Nguyen, Y. Zheng, P. Rosner, M. Benamara, H. P. Strunk, and C. Clerc. Kinetics of Ge growth at low temperature on Si(001) by ultrahigh vacuum chemical vapor deposition. *Journal of Applied Physics*, 97(6):064907, 03 2005.

[20] Geraldine Hallais, Charles Renard, Antoine Barbier, Eric Imbernon, and Nicolas Fourches. Pixel device based on a quantum well: Preliminary results on gate dielectrics. *Nuclear Instruments and Methods in Physics Research Section A: Accelerators, Spectrometers, Detectors and Associated Equipment*, 1047:167906, 2023.

[21] Géraldine Hallais, Gilles Patriarche, Léonard Desvignes, Dominique Débarre, and Francesca Chiodi. Stem analysis of deformation and b distribution in nanosecond laser ultra-doped si:b. *Semiconductor Science and Technology*, 38(3):034003, feb 2023.

[22] G. Bisognin, D. De Salvador, E. Napolitani, M. Berti, A. Carnera, S. Mirabella, L. Romano, M. G. Grimaldi, and F. Priolo. Substitutional B in Si: Accurate lattice parameter determination. *Journal of Applied Physics*, 101(9):093523, 05 2007.

[23] Alex Zunger, S-H Wei, LG Ferreira, and James E Bernard. Special quasirandom structures. *Physical review letters*, 65(3):353, 1990.

[24] Alan R Denton and Neil W Ashcroft. Vegard's law. *Physical review A*, 43(6):3161, 1991.

[25] Lars Vegard. Die konstitution der mischkristalle und die raumfüllung der atome. *Zeitschrift für Physik*, 5(1):17–26, 1921.

[26] Guo-Xu Zhang, Anthony M Reilly, Alexandre Tkatchenko, and Matthias Scheffler. Performance of various density-functional approximations for cohesive properties of 64 bulk solids. *New J. Phys.*, 20(6):063020, 2018.

[27] G Bisognin, D De Salvador, E Napolitani, A Carnera, E Bruno, S Mirabella, F Priolo, and A Mattoni. Lattice strain induced by boron clusters in crystalline silicon. *Semiconductor Science and Technology*, 21(6):L41, apr 2006.

[28] G. Bisognin, D. De Salvador, E. Napolitani, A. Carnera, L. Romano, A.M. Piro, S. Mirabella, and M.G. Grimaldi. Lattice strain of b–b pairs formed by he irradiation in crystalline si1-xbx/si. *Nuclear Instruments and Methods in Physics Research Section B: Beam Interactions with Materials and Atoms*, 253(1):55–58, 2006. Si-based Materials for Advanced Microelectronic Devices: Synthesis, Defects and Diffusion.

[29] M. Kriener, M. S. Bahramy, Y. Tokura, and Y. Taguchi. Enhancement of superconductivity and its relation to lattice expansion in in$_x$Te ($0.84 \leq x \leq 1$). *Phys. Rev. B*, 106:134519, Oct 2022.

[30] Otto Zhou, Qing Zhu, John E. Fischer, Nicole Coustel, Gavin B. M. Vaughan, Paul A. Heiney, John P. McCauley, and Amos B. Smith. Compressibility of m¡sub¿3¡/sub¿c¡sub¿60¡/sub¿ fullerene superconductors: Relation between ¡i¿t¡/i¿¡sub¿c¡/sub¿ and lattice parameter. *Science*, 255(5046):833–835, 1992.

[31] V. V. Brazhkin, E. A. Ekimov, A. G. Lyapin, S. V. Popova, A. V. Rakhmanina, S. M. Stishov, V. M. Lebedev, Y. Katayama, and K. Kato. Lattice parameters and thermal expansion of superconducting boron-doped diamonds. *Phys. Rev. B*, 74:140502, Oct 2006.

[32] Lilia Boeri, Jens Kortus, and O. K. Andersen. Three-dimensional mgb_2-type superconductivity in hole-doped diamond. *Phys. Rev. Lett.*, 93:237002, Nov 2004.

[33] B. Bourguignon, M. Stoica, B. Dragnea, S. Carrez, J. Boulmer, J.-P. Budin, D. Débarre, and A. Aliouchouche. Laser modifications of si(100) : Cl surfaces induced by surface melting: etching and cleaning. *Surface Science*, 338(1):94–110, 1995.

[34] G. Kerrien, M. Hernandez, C. Laviron, T. Sarnet, D. Débarre, T. Noguchi, D. Zahorski, J. Venturini, M.N. Semeria, and J. Boulmer. Optical characterization of laser processed ultra-shallow junctions. *Applied Surface Science*, 208-209:277–284, 2003. Physics and Chemistry of Advanced Laser Materials Processing.

[35] A. Grockowiak. *Supraconductivité et propriétés physiques du silicium très fortement dopé.* PhD thesis, Université de Grenoble - France, 2012.

[36] L. Vincent, F. Fossard, T. Kociniewski, L. Largeau, N. Cherkashin, M.J. Hÿtch, D. Debarre, T. Sauvage, A. Claverie, J. Boulmer, and D. Bouchier. Nanoscale concentration and strain distribution in pseudomorphic films sige/si processed by pulsed laser induced epitaxy. *Applied Surface Science*, 258(23):9208–9212, 2012. EMRS 2011 Spring Symp J: Laser Materials Processing for Micro and Nano Applications.

[37] T. Kociniewski, F. Fossard, J. Boulmer, and D. Bouchier. Synthesis of strained sige on si(100) by pulsed laser induced epitaxy. *Thin Solid Films*, 518(9):2542–2545, 2010. Proceedings of the EMRS 2009 Spring Meeting Symposium I: Silicon and germanium issues for future CMOS devices.

[38] Lam H. Nguyen, V. Le Thanh, D. Débarre, V. Yam, and D. Bouchier. Selective growth of ge quantum dots on chemically prepared sio2/si(001) surfaces. *Materials Science and Engineering: B*, 101(1):199–203, 2003. EMRS 2002 Symposium S: Micro- and Nano-structured Semiconductors.

[39] J.F. Lin, S.S. Li, L.C. Linares, and K.W. Teng. Theoretical analysis of hall factor and hall mobility in p-type silicon. *Solid-State Electronics*, 24(9):827–833, 1981.

[40] José M Soler, Emilio Artacho, Julian D Gale, Alberto García, Javier Junquera, Pablo Ordejón, and Daniel Sánchez-Portal. The siesta method for ab initio order-n materials simulation. *Journal of Physics: Condensed Matter*, 14(11):2745, 2002.

[41] John P Perdew, Kieron Burke, and Matthias Ernzerhof. Generalized gradient approximation made simple. *Physical review letters*, 77(18):3865, 1996.

[42] Axel Van De Walle, M Asta, and G Ceder. The alloy theoretic automated toolkit: A user guide. *Calphad*, 26(4):539–553, 2002.

[43] A Van de Walle, P Tiwary, M De Jong, DL Olmsted, M Asta, A Dick, D Shin, Yi Wang, L-Q Chen, and Z-K Liu. Efficient stochastic generation of special quasirandom structures. *Calphad*, 42:13–18, 2013.